

Bathymetry Retrieval from Hyperspectral Imagery in the Very Shallow Water Limit: A Case Study from the 2007 Virginia Coast Reserve (VCR'07) Multi-Sensor Campaign

CHARLES M. BACHMANN,¹ MARCOS J. MONTES,¹
ROBERT A. FUSINA,¹ CHRISTOPHER PARRISH,²
JON SELLARS,² ALAN WEIDEMANN,³ WESLEY GOODE,³
C. REID NICHOLS,⁴ PATRICK WOODWARD,⁴
KEVIN McILHANY,⁵ VICTORIA HILL,⁶
RICHARD ZIMMERMAN,⁶ DANIEL KORWAN,¹
BARRY TRUITT,⁷ AND ARTHUR SCHWARZSCHILD⁸

¹Naval Research Laboratory, Remote Sensing Division, Washington, D.C., USA

²NOAA NGS, Silver Spring, Maryland, USA

³Naval Research Laboratory, Oceanography Division, Stennis, Mississippi, USA

⁴Marine Information Resources Corporation, Ellicott City, Maryland, USA

⁵U.S. Naval Academy, Physics Department, Annapolis, Maryland, USA

⁶Old Dominion University, Norfolk, Virginia, USA

⁷The Nature Conservancy, Nassawadox, Virginia, USA

⁸University of Virginia, Department of Environmental Science, Charlottesville, Virginia, USA

We focus on the validation of a simplified approach to bathymetry retrieval from hyperspectral imagery (HSI) in the very shallow water limit (less than 1–2 m), where many existing bathymetric LIDAR sensors perform poorly. In this depth regime, near infra-red (NIR) reflectance depends primarily on water depth (water absorption) and bottom type, with suspended constituents playing a secondary role. Our processing framework exploits two optimal regions where a simple model depending on bottom type and water depth can be applied in the very shallow limit. These two optimal spectral regions are at a local maximum in the near infra-red reflectance near 810 nm, corresponding to a local minimum in absorption, and a maximum in the first derivative of the reflectance near 720 nm. These two regions correspond to peaks in spectral correlation with bathymetry at these depths.

Keywords Hyperspectral, shallow-water bathymetry, bottom type, IOP, Hydrolight, Virginia Coast Reserve

Received 26 March 2009; accepted 14 October 2009.

Address correspondence to Charles M. Bachmann, Naval Research Laboratory, Remote Sensing Division, Coastal Science and Interpretation Section, Code 7232, Washington, DC 20375. E-mail: bachmann@nrl.navy.mil

Report Documentation Page				Form Approved OMB No. 0704-0188	
Public reporting burden for the collection of information is estimated to average 1 hour per response, including the time for reviewing instructions, searching existing data sources, gathering and maintaining the data needed, and completing and reviewing the collection of information. Send comments regarding this burden estimate or any other aspect of this collection of information, including suggestions for reducing this burden, to Washington Headquarters Services, Directorate for Information Operations and Reports, 1215 Jefferson Davis Highway, Suite 1204, Arlington VA 22202-4302. Respondents should be aware that notwithstanding any other provision of law, no person shall be subject to a penalty for failing to comply with a collection of information if it does not display a currently valid OMB control number.					
1. REPORT DATE MAR 2009		2. REPORT TYPE		3. DATES COVERED 00-00-2009 to 00-00-2009	
4. TITLE AND SUBTITLE Bathymetry Retrieval from Hyperspectral Imagery in the Very Shallow Water Limit: A Case Study from the 2007 Virginia Coast Reserve (VCR?07) Multi-Sensor Campaign				5a. CONTRACT NUMBER	
				5b. GRANT NUMBER	
				5c. PROGRAM ELEMENT NUMBER	
6. AUTHOR(S)				5d. PROJECT NUMBER	
				5e. TASK NUMBER	
				5f. WORK UNIT NUMBER	
7. PERFORMING ORGANIZATION NAME(S) AND ADDRESS(ES) Naval Research Laboratory, Remote Sensing Division, Washington, DC, 20375				8. PERFORMING ORGANIZATION REPORT NUMBER	
9. SPONSORING/MONITORING AGENCY NAME(S) AND ADDRESS(ES)				10. SPONSOR/MONITOR'S ACRONYM(S)	
				11. SPONSOR/MONITOR'S REPORT NUMBER(S)	
12. DISTRIBUTION/AVAILABILITY STATEMENT Approved for public release; distribution unlimited					
13. SUPPLEMENTARY NOTES					
14. ABSTRACT					
15. SUBJECT TERMS					
16. SECURITY CLASSIFICATION OF:			17. LIMITATION OF ABSTRACT Same as Report (SAR)	18. NUMBER OF PAGES 23	19a. NAME OF RESPONSIBLE PERSON
a. REPORT unclassified	b. ABSTRACT unclassified	c. THIS PAGE unclassified			

Introduction and Background

Numerous institutions, including the Naval Research Laboratory (NRL), have developed look-up tables for remote retrieval of bathymetry and in-water optical properties from hyperspectral imagery (HSI) (Mobley et al. 2005). For bathymetry retrieval, the lower limit is the very shallow water case (here defined to be less than 2 m), a depth range that is not well resolved by many existing bathymetric light detection and ranging (LIDAR) sensors such as Scanning Hydrographic Operational Airborne Lidar Survey (SHOALS) (Ebrite, Pope and Lillycrop 2001). The ability to rapidly model these shallow water depths from HSI directly has potential benefits for combined HSI/LIDAR systems such as the Compact Hydrographic Airborne Rapid Total Survey (CHARTS) (Smith, Irish and Smith 2000). Among the many potential application areas is the National Oceanic and Atmospheric Administration (NOAA) LIDAR shoreline mapping initiative (White 2007), in which shallow-water topo/bathy datasets with seamless coverage in an alongshore swath encompassing the intertidal zone can be used for extraction of both mean lower low water (MLLW) and mean high water (MHW) shoreline. In this study, we focused on the validation of a near infra-red feature corresponding to a local minimum in absorption (and therefore a local peak in reflectance), which can be correlated directly to bathymetry with a high degree of confidence. Our study also concludes that a second near infra-red feature near a peak in the derivative of the reflectance is another optimal region for retrieval in the very shallow limit. Compared to other VNIR wavelengths, these particular near-IR features correspond to a peak in the correlation with depth in this very shallow water regime. In this article, we develop a simplified computational framework that exploits these near infra-red features and the fact that in the near infra-red, in the very shallow water limit, reflectance depends primarily on water depth (water absorption) and bottom type, with suspended constituents playing a secondary role.

The general problem of bathymetry retrieval from HSI is more complicated out of these limits. At visible and near infra-red (VNIR) wavelengths, reflectance is determined by a variety of factors including water depth, bottom type, and the presence of suspended constituents such as color-dissolved organic matter (CDOM), suspended sediments, chlorophyll, phytoplankton, and other suspended constituents (Mobley 1994). The general problem of retrieving depth and other water properties has been approached using spectral look-up tables (Mobley et al. 2005) in which a forward radiative transfer model such as Hydrolight (Mobley and Sundman 2000) is executed repeatedly with varying water column properties, depth, and bottom types. To be comprehensive, these look-up tables must be large and may need to be tuned to specific coastal types because of differences in bottom types and water properties, which may vary significantly with coastal type. Other approaches to the problem of bathymetry retrieval from HSI have included a semi-analytical model (Lee et al. 1999, 2001). Both the LUT approach and semi-analytical models simultaneously retrieve more than one inherent optical property (IOP) of the water column.

Recent commercial bathymetric LIDAR systems, such as the SHOALS (Ebrite, Pope and Lillycrop 2001), have been designed for improved performance at the deep end of the operating range, possibly at the expense of limiting performance in shallow water (0–4 m depth). In particular, the combination of a relatively large (several nanosecond) laser pulse width (which increases the length of the total system response function), large spot size at the water surface (due to design requirements imposed by eye safety considerations with high-powered lasers), and geometric pulse stretching at the water surface (largely due, in the case of the SHOALS, to a fixed 20° incidence angle) make it difficult to resolve the bottom in returns from very shallow water (less than ~2 m). Typical data gaps found in

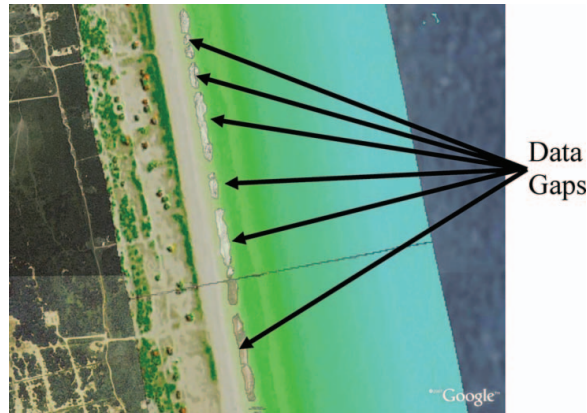


Figure 1. Typical SHOALS bathymetry coverage superimposed on a Google Earth image. These data were collected by the U.S. Army Corps of Engineers in Currituck County, N.C., in July 2004. The sensor fails to resolve the bottom in returns from very shallow water regions, leading to data gaps.

many of the SHOALS standard products are shown in Figure 1. Some fairly recent studies have focused on using advanced digital signal processing techniques to estimate bottom depths from LIDAR waveforms in these very shallow regions, with encouraging results (Yang et al. 2007). However, a large number of existing SHOALS datasets exhibit data gaps, such as those shown in Figure 1. In addition, the very low (few hundred meter) altitude required for data acquisition by bathymetric LIDAR systems makes acquisition impossible in many regions of the world. In this article, we focus on this very shallow water regime, specifically on the retrieval of bathymetry from a spectral range where a relatively simple model for reflectance can be assumed and where a full-scale LUT may not be necessary. Compared to the reflectance at visible wavelengths, where all contributions from the water column must be carefully considered, near infra-red wavelength reflectance (beyond 800 nm) is primarily dependent on water absorption and depth, along with bottom reflectance, with water column constituents playing a secondary role. We will find that a near optimal wavelength for this retrieval is approximately 810 nm. A second optimal region also appears near a peak in the first derivative of the reflectance near 720 nm.

Water Column Reflectance in the Near Infra-Red and Hydrolight Models

In this section, we demonstrate that varying concentrations of suspended constituents do not significantly affect the reflectance at 810 nm or 720 nm but indeed are a large contributing factor to the shorter wavelength returns. Likewise, the wavelength ranges near 810 nm and 720 nm are particularly sensitive to water depth in the very shallow limits. To demonstrate this theoretical expectation, we have run a series of models using Hydrolight. This model allows the user to vary the concentration of constituents, bottom type, depth, and other parameters and look at their contribution to remote sensing reflectance as a function of wavelength. Hydrolight supports the ingest of field measured spectra. To test our model assumptions, a bottom reflectance measured by us in the intertidal zone at the Virginia Coast Reserve Long-term Ecological Research (VCR LTER) site (<http://www.lternet.edu/sites/vcr/>) was used as a model input to Hydrolight. Total suspended sediment (TSS), CDOM, and chlorophyll concentration were held constant with values

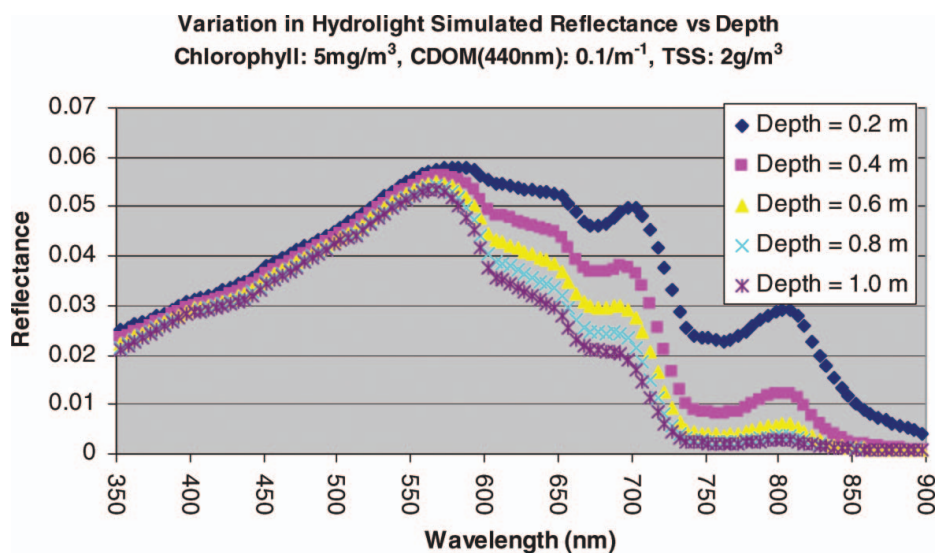


Figure 2. Hydrolight modeled reflectance for varying depths with fixed water column properties. Input bottom reflectance was from an ASD in situ measurement over an oyster shell bottom in Figure 6.

that might be found in coastal lagoons such as those at the VCR LTER. With the water column properties fixed, depth was varied, and the resulting reflectance was calculated from Hydrolight. Figure 2 shows the resulting reflectance for a fixed set of water column properties as the depth is varied. It also shows a peak in the vicinity of 810 nm that is well correlated with depth. The spectral region near 720 nm (maximum derivative of reflectance) is another peak in this correlation. Empirical studies of the visible and near IR spectrum in laboratory settings have shown a relatively broad peak near 810 nm, corresponding to a local minimum in the liquid water absorption (Curcio and Petty 1951).

We also used Hydrolight to show that varying suspended constituents are indeed expected to make only a small difference near 810 nm and 720 nm, while at shorter wavelengths in the visible, these changes have a significant impact that cannot be ignored in modeling. Figure 3a illustrates this point for a case in which total suspended sediment (TSS) is varied while all other inherent optical properties (IOPs) are held fixed and the depth is constant for a specific bottom type (in this case, the field spectrum of our bottom substrate taken for the oyster shell bottom site at Wreck Island, Virginia, described later in this article). We provide two examples, one at a fixed depth of 0.4 m and the other at 0.8 m. Hydrolight reflectances are shown for TSS = 2, 3, and 5 g/m³. Note the much larger variation in reflectance at wavelengths below 700 nm compared to longer wavelengths.

While the total contributions to reflectance are governed by the equations of radiative transfer (Mobley 1994) and are included in Hydrolight, the Hydrolight simulations suggest the possibility of an approximate form in this wavelength regime. The simulations of Figures 2 and 3 show that in the longer wavelengths, the dominant factor is the absorption due to liquid water, with the influence of the scattering becoming a negligible term. Under these assumptions, and ignoring fluorescence and Raman scattering for the moment, the attenuation is approximately due to two terms: one due to the reflectance of the bottom and one due to the properties of the water column with the second becoming smaller in the near

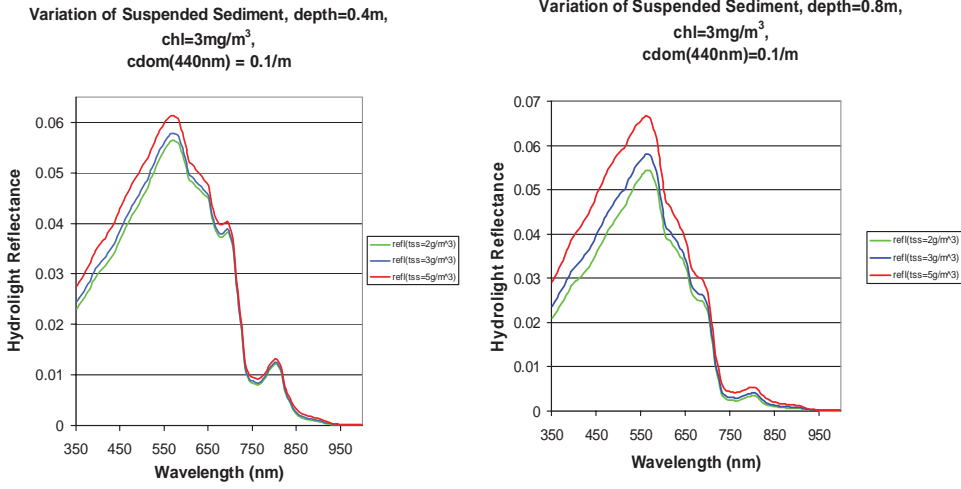


Figure 3a. Simulated reflectance using Hydrolight, for varying TSS, with all other IOP's held fixed, and at fixed depths: (left) 0.4 m, (right) 0.8 m.

infra-red wavelengths:

$$R_{\lambda} \sim \rho_{\text{bottom}} e^{-\alpha(\lambda)d} + R_{\infty}(\lambda)(1 - e^{-3\alpha(\lambda)d}) \quad (1)$$

where R_{λ} is the reflectance at wavelength λ ; ρ_{bottom} is the bottom reflectance; $\alpha(\lambda)$ is a wavelength-dependent attenuation coefficient, which at longer near infra-red wavelengths is dominated by the absorption due to liquid water and is less affected by scatter as shown in the Hydrolight simulations; d is the depth (for our purposes we define quantities such that d is in cm and $\alpha(\lambda)$ is in cm^{-1}); and $R_{\infty}(\lambda)$ is a reflectance of the water column when there is no bottom contribution. At longer near infra-red wavelengths, $R_{\infty}(\lambda)$ is near zero, whereas at shorter wavelengths this term is significant due to the scattering of suspended constituents. Eq. (1) is similar to approximate forms for these two contributions found, for example, in Lee et al. (1994), where $\alpha(\lambda)$ is a composite of factors such as the quasi-diffuse attenuation coefficient (sum of absorption and scattering coefficients) and the downwelling distribution function. With this assumption, we look for a regression between $\ln(R_{\lambda})$ and d , assuming that in our shallow water limit the first term in Eq. (1) is the most significant. In this approximation, we have:

$$\ln(R_{\lambda}) = -\alpha(\lambda)d + \beta(\lambda) \quad (2)$$

where $\beta(\lambda) \sim \ln(\rho_{\text{bottom}})$ is a wavelength-dependent offset, depending on the bottom reflectance.

Numerically, we can show that this is further justified by extending the Hydrolight simulations in Figures 2 and 3a to deeper depths. Figure 3b shows $\ln(R_{\lambda})$ versus d (in meters) for $\lambda = 722.5 \text{ nm}$ and 812.5 nm , near the two optimal wavelengths for this type of retrieval. In this figure we have plotted the effects of increasing the concentration of TSS and chlorophyll. The relationship between $\ln(R_{\lambda})$ and d is linear in the shallow limit, and departure from this linear limit varies depending on concentrations of TSS and chlorophyll. More important, the linear slope is the same regardless of concentration, and the point of departure from linearity marks the point at which the second term in Eq. (1) due to

the water column becomes more significant and can no longer be neglected. The departure from linearity occurs sooner at higher concentrations of suspended constituents as scattering and absorption become more important. Even at low concentrations, extinction eventually

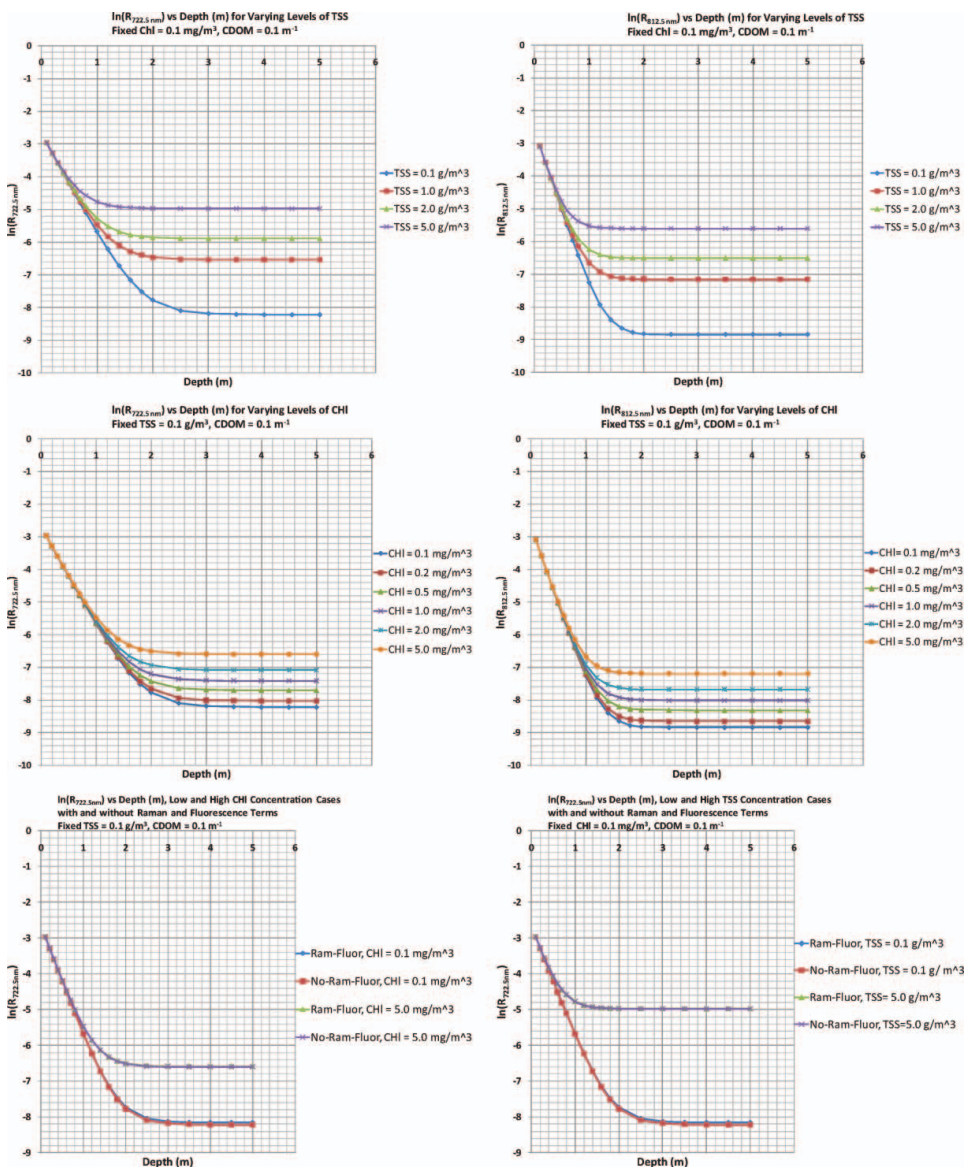


Figure 3b. Hydrolight simulations showing the natural logarithm of reflectance vs. depth in meters at two NIR wavelengths: 722.5 nm (left column) and 812.5 nm (right column) for varying levels of total suspended sediment (TSS) at low, fixed chlorophyll and CDOM concentrations (top row), and for varying levels of chlorophyll concentration at fixed TSS and CDOM concentrations (middle row). (Bottom row) Negligible impact of fluorescence and Raman scattering for (bottom, left) low and high concentrations of chlorophyll and (bottom, right) low and high concentrations of TSS at 722.5 nm.

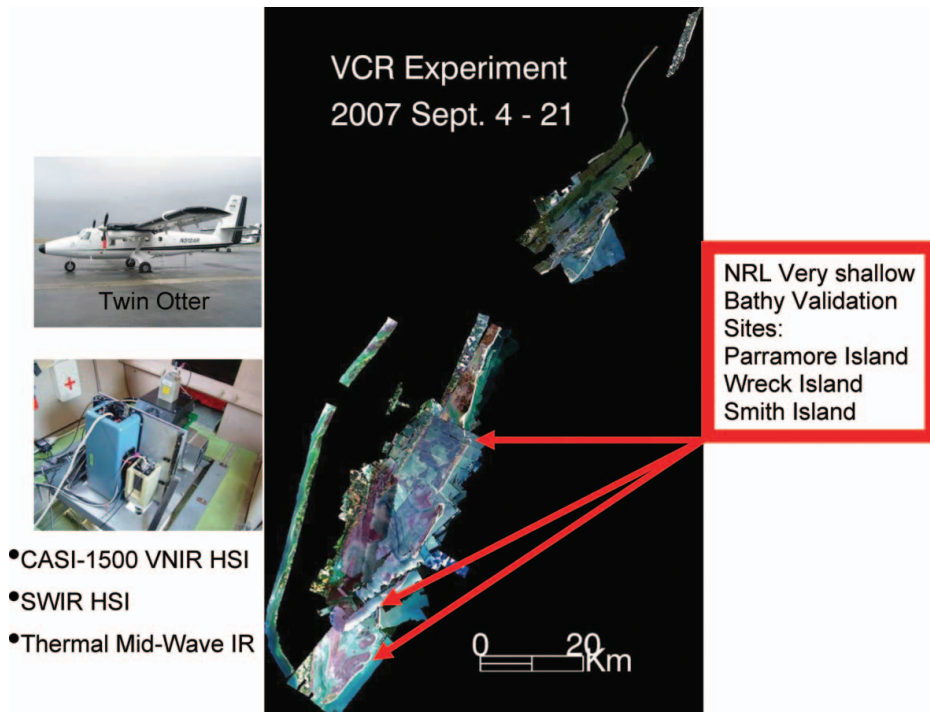


Figure 4. NRL CASI-1500 quick look composite of the VCR'07 multi-sensor campaign. The sensor suite covered over 1880 km², some areas multiple times at different tidal stages. Areas used for shallow water bathymetry validation during the VCR'07 campaign and earlier in 2005 are indicated by red arrows.

becomes the most important factor at these longer NIR wavelengths, which is why the curves reach an asymptotic limit in all cases. TSS has the biggest impact on the depth of departure from linearity in these curves, while chlorophyll has an impact but not as strong. There is virtually no dependence on CDOM concentration at these NIR wavelengths, so these graphs are not shown. Finally, the impact of fluorescence and Raman (inelastic) scattering is negligible as shown in Figure 3b. For this reason, the fluorescence and Raman terms were ignored in the discussion surrounding Eq. (1).

Virginia Coast Reserve 2007 (VCR'07) Campaign

During September 2007, the Naval Research Laboratory (NRL) and a number of collaborating institutions undertook a multisensor airborne data collection and *in situ* validation campaign at the Virginia Coast Reserve (VCR'07). Airborne, in-water, and land-based measurements took place over the course of the 2–1/2 week exercise and covered a 95 km stretch of barrier islands, inlets, coastal lagoons, tidal flats, and mainland marsh systems. In all, some 1880 km² were covered by the NRL sensor suite (Figure 4), some areas multiple times at different tidal stages. NRL flew three sensors on a Twin Otter aircraft: a Compact Airborne Spectrographic Imager (CASI-1500), which is a visible and near infra-red (VNIR) HSI sensor (www.itres.com); a Surface Optics (www.surfaceoptics.com) InGaAs SWIR HSI sensor operating in the 0.9–1.7 μm spectral region; and a single-

channel Indigo Systems Merlin midwave IR camera operating in the 3–5 μm spectral range (www.corebyindigo.com/products/legacy.cfm). This article focuses on the CASI imagery taken during the experiment and the *in situ* validation data collected to study the NIR feature described earlier. Other littoral focus areas studied during the VCR'07 experiment included the remote retrieval of soil bearing strength (Bachmann et al. 2008), biomass retrieval, land-cover mapping (Bachmann et al. 2003), and seagrass and oyster reef monitoring.

During the experiment, the NRL CASI-1500 was operated at an altitude of approximately 3000 m, with a nominal ground sample distance (GSD) of roughly 1.5 m. At this spatial resolution, the swath width was approximately 2.25 km. Although the CASI-1500 is capable of up to 288 spectral channels, spectral data were binned to 96 channels to improve signal to noise ratio (SNR). With this number of channels, the spectral bins had a size of approximately 7 nm. Since the CASI-1500 hyperspectral imagery was acquired in a coastal region, with water present in every scene, data were taken in a manner that would minimize glint by confining data collection to specific windows when the solar elevation angle was in the range between 30 and 60°. A further measure to reduce glint was that flight line headings during data acquisition were either into or out of the sun. This was accomplished by sets of lines in hourly windows in such a way that followed the average heading into or out of the sun for the window.

For the very shallow bathymetry study, field validation efforts used Analytical Spectral Devices (ASD) spectrometers (www.asdi.com) positioned on a tripod in a shallow cove on the northwestern shore of Wreck Island, Virginia, and in the shallow stretches of a muddy tidal creek and salt marsh system in the northern end of Parramore Island, Virginia. Depth and ASD spectral measurements were recorded on a falling tide until the substrate was completely exposed, allowing an *in situ* bottom reflectance to be obtained in the measurement suite. Bottom reflectance was also measured by divers using an underwater spectrometer at other locations. Previously, during field work in October 2005, ASD measurements had been collected in the shallow waters on the edge of a salt marsh system in the northern end of Smith Island. The ground truth for VCR'07 included postprocessed kinematic (PPK) GPS data for the inter-tidal region on the northern end of Wreck Island to support product validation. In addition, depth soundings were taken in the shallow waters behind the island and in the adjacent channel separating Wreck from Cobb Island. At the conclusion of the study, the NASA Experimental Airborne Advanced Research LIDAR (EAARL) acquired data in conjunction with the NRL sensor suite, albeit during a period when weather conditions were not optimal and turbidity was high. For this study, the PPK GPS ground truth data served as the elevation reference data for bathymetry retrieval validation.

Figures 5 and 6 show the measured spectral curves for each depth collected during the measurement cycle at Parramore and Wreck Islands, respectively, during VCR'07, along with *in situ* photos and the regression at 810 nm. A similar regression was carried out for data taken by us on the northern end of Smith Island, Virginia, in October 2005 (Figure 7) for a sand/silt bottom on the watery margin between beach and salt marsh zones. As described earlier, the focus was on the longer wavelengths of the near infra-red spectrum, but the full range spectrum from 0.35–2.5 μm also was collected. The visible and near infra-red are the portions of the spectrum usually used in water applications, since the reflectance beyond a micron is near zero, except when constituents in the water column are fully mixed to the surface layer. The visible shallow water spectra in Figures 5, 6, and 7 show a relatively broad peak near 810 nm, corresponding to a local minimum in the liquid water absorption (Curcio and Petty 1951). There is a similar peak near 1.076 μm , which is of a similar origin, though of a less pronounced character.

To assess the relative merits of wavelength selection at these longer wavelengths and confirm the optimality of the choice of the 810 nm and 722 nm features, we computed an R^2 goodness of fit between a linear regression of $\ln(R_\lambda)$ and d , where R_λ is the reflectance at wavelength λ and d is the depth in cm. This is based on our earlier assumption that the bottom type and water absorption and depth are the most significant factors in the very

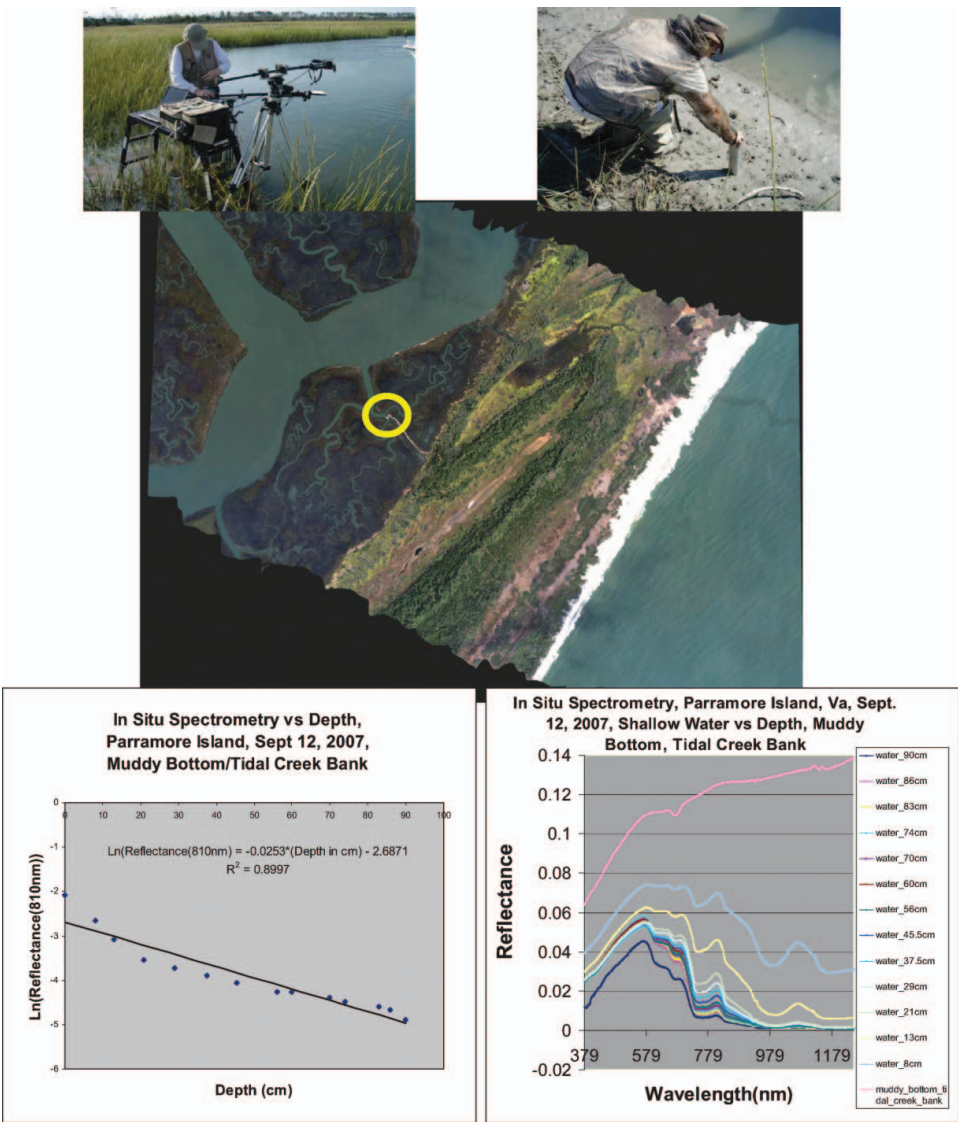


Figure 5. (Top) Parramore Island in situ spectrometry site on salt marsh tidal creek bank, September 12, 2007, with muddy bottom; (middle) NRL CASI 1500 image of Parramore Island on same day, showing the ASD spectral measurement site (yellow circle) where spectral reflectance vs. depth profiles were recorded: (top, left) beginning (near high tide) (top, right) and end (near low tide) of measurement cycle. (Bottom right) Spectral samples at depths varying from 90 cm to 0 cm (wet substrate). (Bottom, left) $\ln(R_{810\text{nm}})$ vs. d (depth in cm).

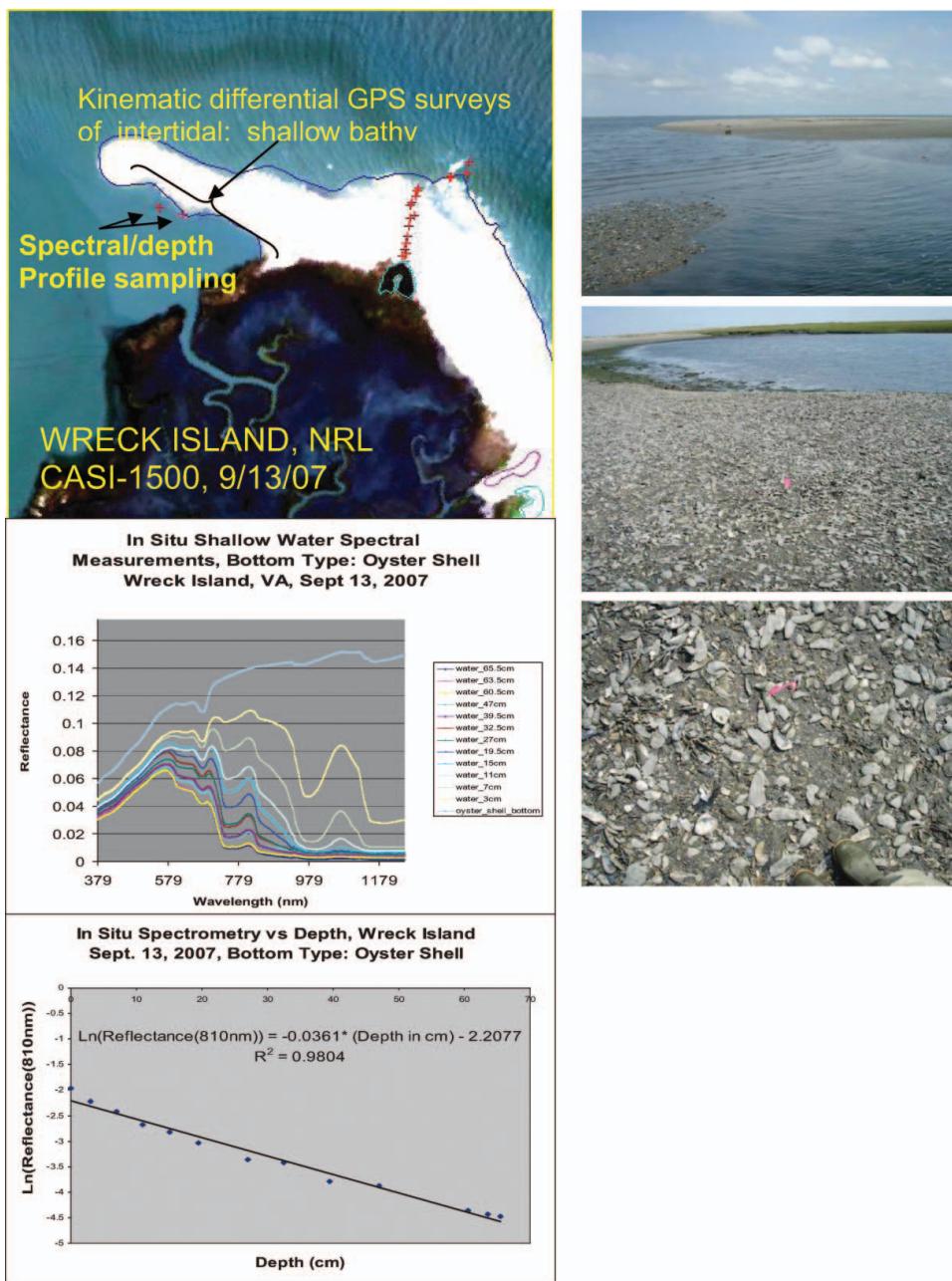


Figure 6. Wreck Island in situ spectrometry site with oyster shell bottom mixed with sand/silt in a shallow cove. (Top, left) sampling sites for oyster shell site (3 top right photos) and second site with *Ulva lactuca* (not shown) on NRL CASI imagery taken on the same day. (Middle, left) Spectral samples at depths varying from 65.5 cm to 0 cm (wet substrate) for the oyster shell site. (Bottom left) $\ln(R_{810\text{nm}})$ vs. d (depth in cm) and associated regression for the oyster shell site.

shallow water regime in the near infra-red, and this assumption is supported by the results of our Hydrolight simulations in Figures 2, 3a, and 3b in this wavelength and depth range.

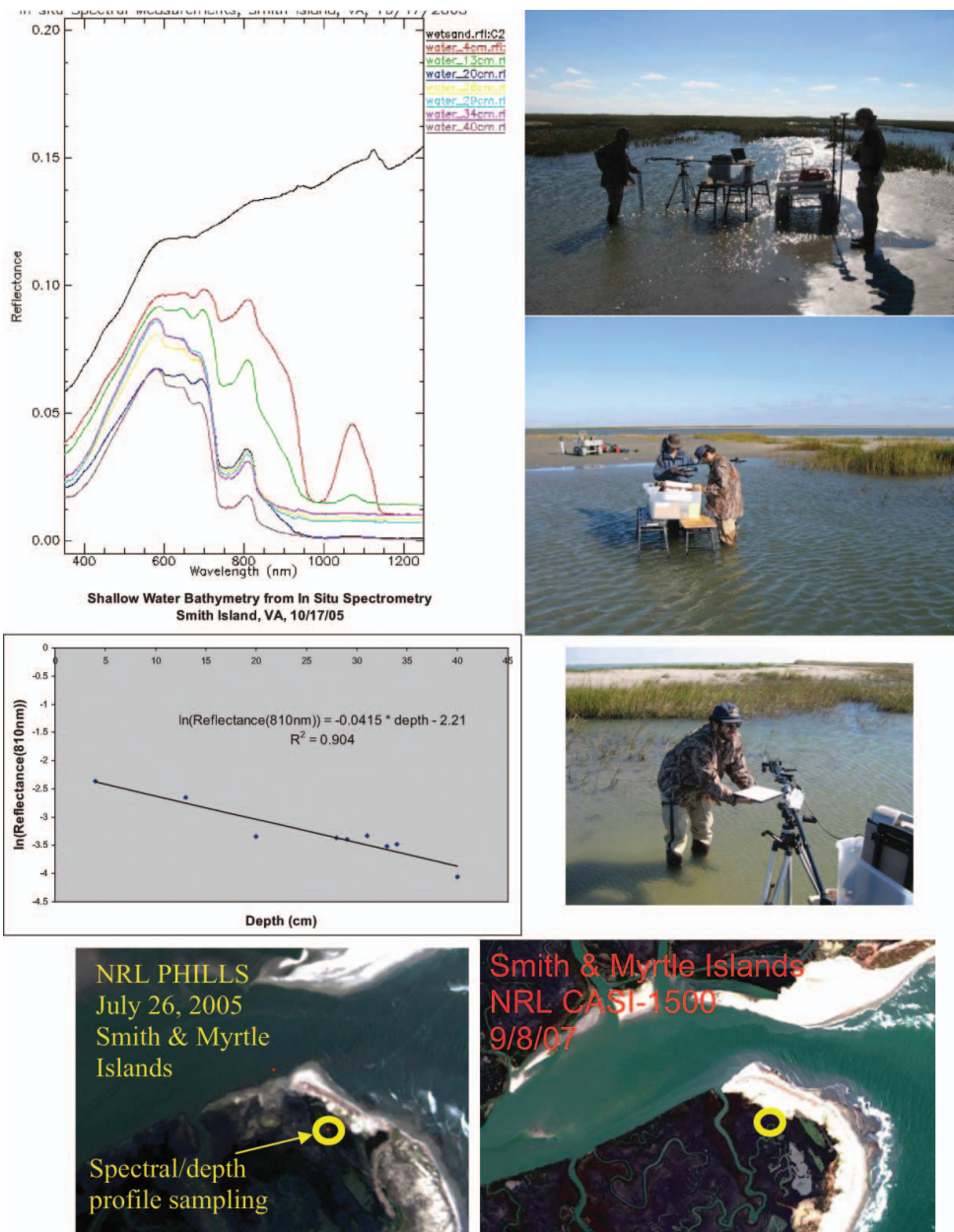


Figure 7. In situ spectral measurements initially carried out on the northern end of Smith Island, Va., in October 2005 over a sand/silt bottom. (Top and middle right) Site photos. (Top, left) spectral reflectance curves measured by the ASD spectrometer, (top, right) site photos of spectrometer, (middle, left) $\ln(R_{810\text{nm}})$ vs. d (depth in cm), (bottom, left) NRL PHILLS HSI image of this region taken in July 2005 showing sample location; (bottom, right) the same area image on September 8, 2007, during the VCR'07 campaign.

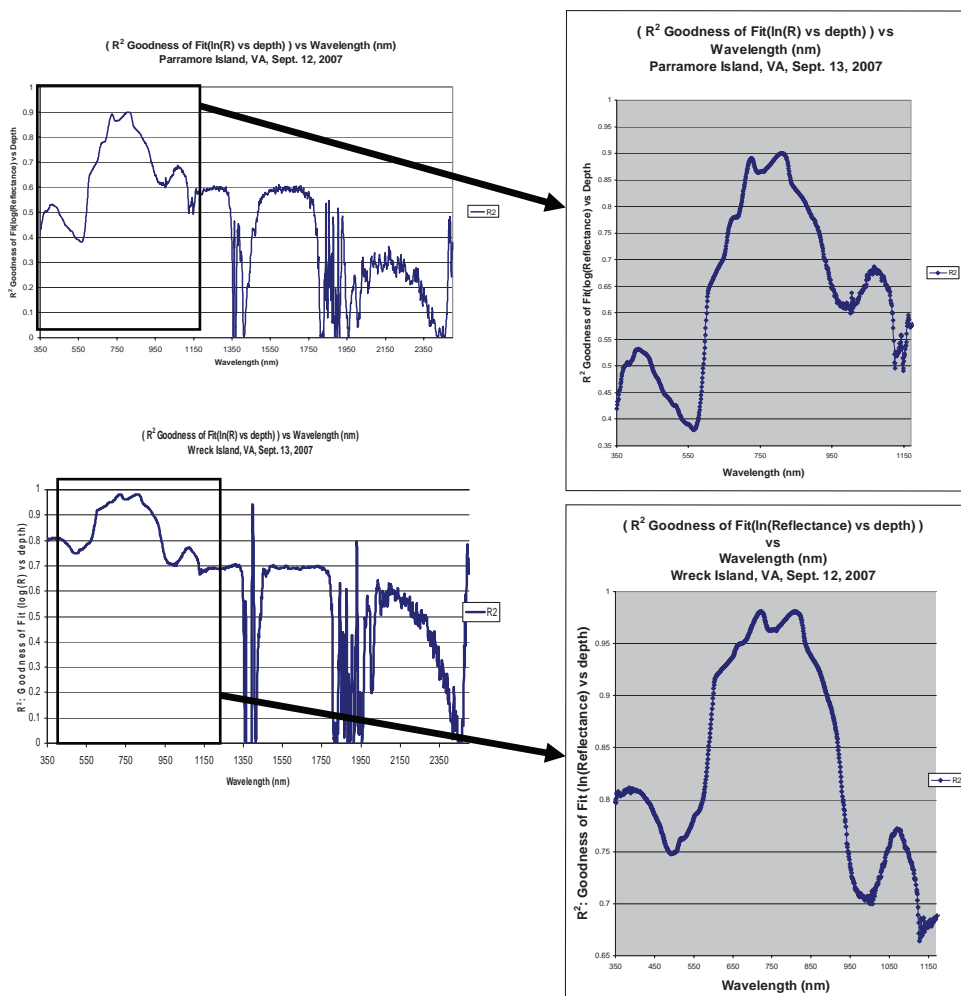


Figure 8. R^2 fit of $\ln(R_x)$ and d for: (top row) Muddy bottom, Parramore Island, (bottom row) oyster shell bottom, Wreck Island. (Left column) 0.35–2.5 μm , (right column) enlargement of 0.35–1.07 μm .

Figure 8 shows plots of this feature across the full spectrum for the Parramore Island and Wreck Island sites in Figures 5 and 6, with enlargements of the VNIR portion of the spectrum. The best correlation occurs near two peaks, one at 810 nm and the other near 720 nm. The feature at 720 nm corresponds to a steep slope in the NIR, making it more sensitive to change than other portions of the NIR, while the 810 nm feature corresponds to a local minimum in water absorption and thus a local maximum in reflectance that is apparent in very shallow waters. In this article, we concentrate on the 810 nm feature, although the 720 nm feature also could be used. However, the Hydrolight simulations of Figures 3a and 3b suggest that the 720 nm feature may be useful to slightly deeper depths; the primary reason appears to be that the extinction at 720 nm is not as strong as 810 nm and the effect of suspended concentration appears to be stronger at 810 nm than at 720 nm, leading to departures from a linear relationship at shallower depths (by as much as 20 cm).

For practical measurements either with a portable spectrometer or an imaging spectrometer from the air, the difference in extinction also means that the noise floor will be reached sooner at 810 nm than at 720 nm. Wavelengths between these two peaks would work well also, but the best fit with R^2 values near 0.89 (muddy bottom) and 0.98 (oyster shell bottom) for Parramore Island and Wreck Island, respectively, are near these two wavelengths. In the VNIR spectrum below 800 nm, for the oyster shell bottom case (Wreck Island), R^2 never exceeds ~ 0.81 (at 384 nm) compared with the peaks at 721 nm and 809 nm where $R^2 \sim 0.98$, while for the muddy bottom case (Parramore Island) the R^2 never exceeds ~ 0.53 (at 409 nm) compared with the peaks at 725 nm ($R^2 = 0.891$) and 811 nm ($R^2 = 0.900$). Spectral stability and high R^2 of the 810 nm feature and the wavelength range near the steep slope at 720 nm for both dark and bright bottom cases demonstrate the optimality of these two NIR wavelength regions. In contrast, at visible wavelengths, the best R^2 is not at a stable location and is only moderately good for brighter bottoms.

Bathymetry Retrieval

During VCR '07, the NRL CASI-1500 acquired imagery over Wreck Island at eight different times. Two of these scenes were acquired on the same day and during the sampling window for *in situ* spectral sampling on Wreck Island on September 13, 2007. The first of these scenes was acquired on a falling tide roughly 15 minutes prior to the first ASD spectral sampling (Figure 6). Although various atmospheric correction models were explored using the NRL *Tafkaa* atmospheric correction program (Montes et al. 2004), an empirical line calibration was ultimately used, aligning the spectral data from the CASI with ASD data taken both in the water (dark pixel) for the depth versus ASD spectral profiles and with those ASD spectral data that were acquired by us for substrate studies (Bachmann et al. 2008) on the beach nearby (bright pixels).

Figure 9 shows a flow diagram for NRL's very shallow water bathymetry retrieval. Data were initially segmented using scene-based regions of interest designed to separate out the deep water pixels from shallow water pixels. This step involved maximum likelihood classification to trim off deep water pixels from the scene. For the remaining shallow water data, prior to applying the 810 nm regressions, the data were partitioned by bottom type using spectral angle mapper (Kruse et al. 1993) criterion which matched the CASI imagery pixels to the closest ASD profile found in the *in situ* profiles taken by NRL during VCR '07 and in October 2005. During this phase of the processing, a moderate angle was sufficient to generate a reasonable delineation of bottom types in the scenes. Three bottom types described earlier, oyster shell bottom, muddy bottom, and sand/silt mixture, were used and were based on the ASD versus depth profile spectral libraries obtained at Parramore, Wreck, and Smith Islands. Retrievals using the $\ln(R_\lambda)$ vs. d regressions for the 810 nm for each bottom were applied separately to the data after segmentation by bottom type. The resulting depth retrieval in centimeters is shown in Figure 10. Although the bathymetry retrieval is real-valued, in Figure 10 the retrieval has been quantized (see the accompanying color bar) to better highlight bathymetric structure; Figure 10 also shows some examples of bathymetry profiles from the retrieval without the application of the color quantization applied for visualization purposes. The bathymetry retrieval is applied successfully in the shallow cove, the shallow ocean side in the surf zone, as well as in the salt marsh and tidal creeks in the western portion of the image. The salt marsh vegetation is dominated by *Spartina alterniflora*, an erectophile canopy that allows for significant substrate exposure, and when inundated, a significant fraction of the pixel appears as water in a nadir view.

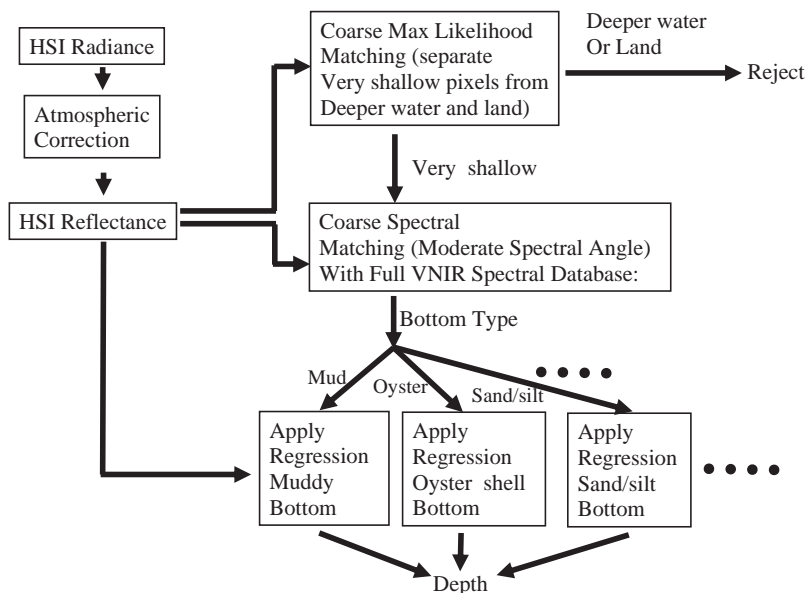


Figure 9. Processing chain for very shallow water bathymetry retrieval.

This allows the 810 nm retrieval to be used successfully in these regions via the muddy bottom regression.

Accuracy Assessment

Our goal for this experiment was to achieve an estimated error of within 10–15 cm of true depth. In order to establish the accuracy of our approach, a differential GPS survey of the cove area (Figure 11) at the north end of Wreck Island was undertaken during the measurement of the depth versus reflectance profile for the oyster shell bottom in this cove. Position and elevation data were obtained by postprocessing kinematic GPS data collected by NOAA's National Geodetic Survey (NGS) throughout the morning and early afternoon on September 13, 2007. A dedicated GPS base station in the project area was used, and baselines were limited to < 2 km. The waterline was periodically surveyed and GPS position and elevation throughout the exposed region of the cove were surveyed as the tide fell. Depth at the time of the NRL CASI overflight at 9:45 A.M. (local time: UTC -4) was retrieved using the method described above, and a track of the survey zone is depicted in Figure 11. Figure 12 compares the depth established by the GPS survey with that based on our bathymetry retrieval method, both as a scatterplot and with the results binned to show mean and standard deviation of our retrieval. A line representing an ideal result is also provided for reference. Notice that the result remains within one standard deviation of the ideal case out to about 1 m. For depths ranging from 0–1 m, the root mean square error (RMSE) is 13.7 cm, within our established goal for uncertainty.

The retrieval based on the 810 nm feature diverges from the true depth just beyond 1 m. This is due to two factors: (a) scattering and absorption by the suspended constituents can no longer be ignored beyond this depth in the concentrations found in the VCR waters and (b) extinction at this wavelength also begins to dominate. Both of these effects lead to departure from a linear relationship between the logarithm of reflectance and depth, as

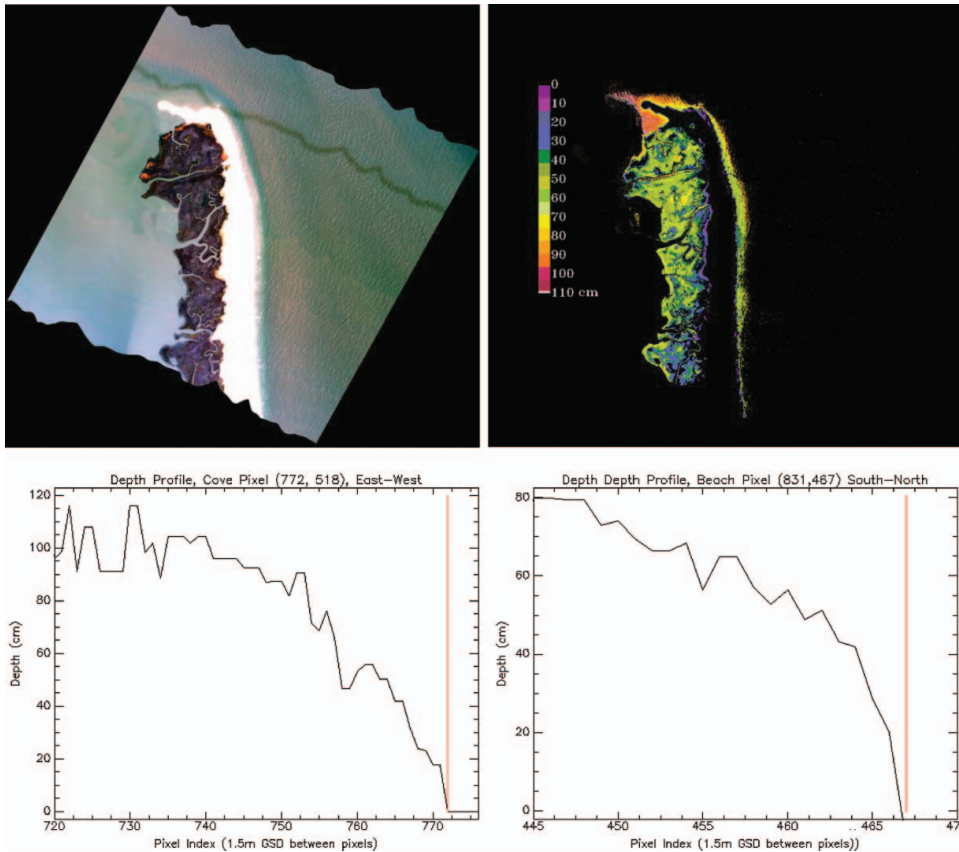


Figure 10. (Left) NRL CASI-1500 image of Wreck Island (9:45 AM line). (Right) Retrieved depth using the 810 nm regressions for each bottom type determined in preprocessing from the spectral libraries. Depth is quantized in the color scale, but retrieval is continuous; (right) typical depth profiles from this bathymetry retrieval (left) in the cove in the northwest region of the image where sampling was performed (see Figure 6) and (right) on the beach on the eastern side of the island.

predicted by the Hydrolight simulations. The fact that the 810 nm feature has become too attenuated at depths beyond this level also means that, practically speaking, the response of the sensor is no longer distinguishable from the noise floor of the CASI hyperspectral sensor. There is an abrupt fall-off in the accuracy of the retrieval, resulting from the fact that the 810 feature at depths of 1 m and beyond are all approximately the same, causing the retrieval to level off at an estimated value of 1 m at this depth and deeper. Note that the 720 nm feature may indeed produce a more accurate retrieval out to deeper depths because it does not reach this noise floor as quickly with depth as the 810 nm feature does and is not quite as sensitive to concentration of suspended constituents (Figure 3b).

Contributions to the error shown in Figure 12 stem from several sources. One is the potential for error in the radiometric accuracy which depends on such factors as accurate instrument calibration and atmospheric correction. These uncertainties result in errors in the observed reflectance, in this case at the 810 nm feature used in the model, and introduce the potential for errors in the bottom type discrimination earlier in our processing framework in Figure 9. The uncertainty in the 810 nm reflectance feature δR_{810} can be assessed through

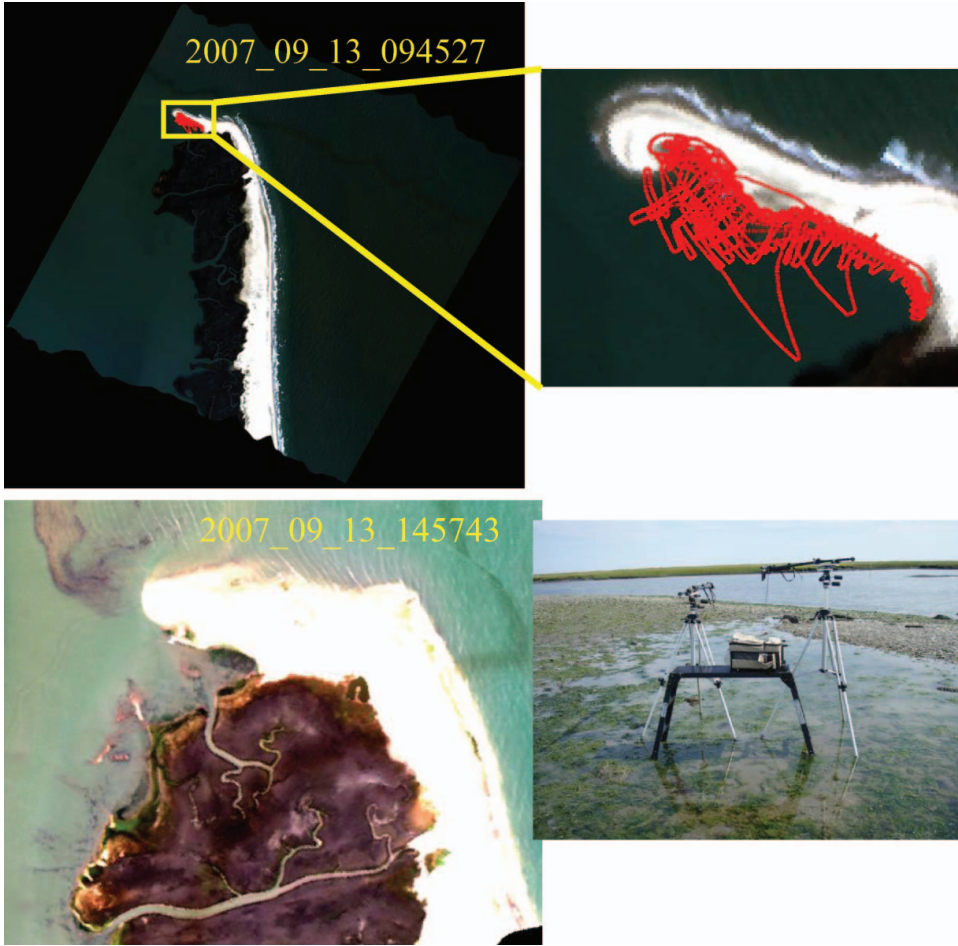


Figure 11. (Top, left) NRL CASI Image of the north end of Wreck Island on September 13, 2008, from flight line begun at 09:45:27 with superimposed track of the differential GPS survey of the cove at the northern end of Wreck Island. This area was used for validation of the bathymetry retrieval using the GPS data. (Bottom left) Image taken near low tide later that same day. Green areas in the cove are from *Ulva lactuca* (sea lettuce) on the surface. ASD depth profiles of this substrate (bottom right) were incomplete due to insufficient instrument battery life and were not included in the retrieval models of this article.

error propagation of the fundamental equation of the regression in Eq. (2):

$$(\delta d)_{R_{810}} = \frac{1}{\alpha(810)_{bottom}} \frac{\delta R_{810}}{R_{810}} \quad (3)$$

To get an idea of the potential impact of this term, consider, for example, that for a radiometric error of 20% in the reflectance, that is, $(\delta R_{810}/R_{810}) = 0.2$, we would obtain an error in depth of $(\delta d)_{R_{810}} \approx 7.9$ cm for the muddy bottom case (Figure 5), while for the oyster shell bottom case (Figure 6), we would obtain $(\delta d)_{R_{810}} \approx 5.5$ cm, and the sand/silt bottom case (Figure 7), we find $(\delta d)_{R_{810}} \approx 4.8$ cm. A 10% radiometric error would lead to an error of 3.95, 2.77, and 2.41 cm, respectively. In general, the brighter the bottom, the

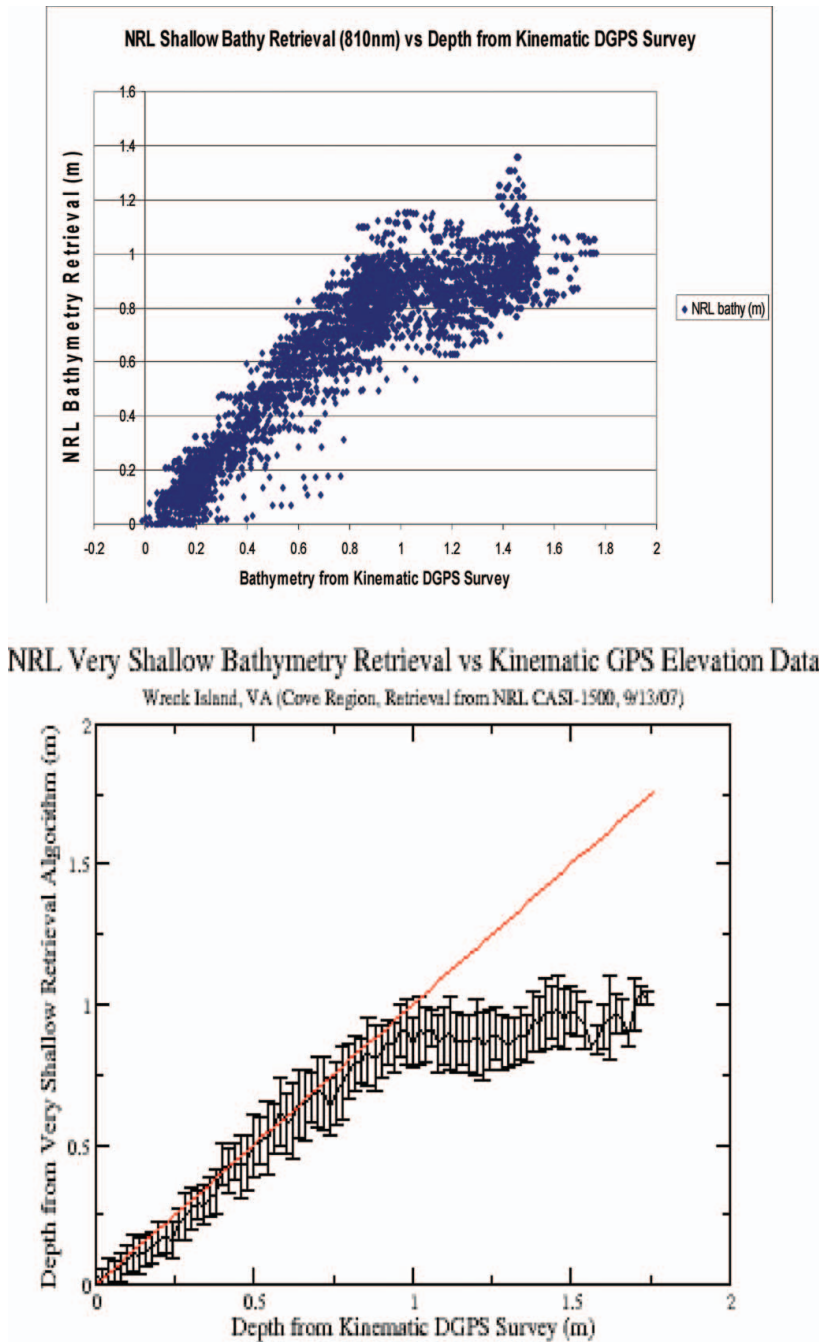


Figure 12. (Top) Scatterplot of depth determined from GPS survey of the intertidal zone vs. very shallow water bathymetry retrieval using the approach in Figure 9 in the cove on Wreck Island. (Bottom) Binned result showing mean and standard deviation of retrieval vs. depth determined from the kinematic differential GPS survey compared against the ideal case.

lower the error rate for this term. Thus, the brighter sand/silt bottom of Figure 7 results in the lowest estimated error of the three measured, while a bottom with SAV, such as *Ulva lactuca* (sea lettuce) or seagrass might be somewhere in between the estimated errors obtained for the three bottom types measured in this study.

Another potential source of error is the inaccuracy in the bottom type selection, which is a critical part of our processing approach depicted in Figure 9. For this source of error, there are two related terms to consider since both regression coefficients in Eq. (2) depend on the bottom type. Using this equation, when we propagate errors, we find (up to a sign) that:

$$(\delta d)_{\alpha(\lambda)_{\text{bottom}}} = \frac{(\beta_{\text{bottom}} - \ln(R_\lambda))\delta\alpha(\lambda)_{\text{bottom}}}{\alpha^2(\lambda)_{\text{bottom}}} = d \cdot \frac{\delta\alpha(\lambda)_{\text{bottom}}}{\alpha(\lambda)_{\text{bottom}}} \quad (4)$$

$$(\delta d)_{\beta(\lambda)_{\text{bottom}}} = \frac{\delta\beta(\lambda)_{\text{bottom}}}{\alpha(\lambda)_{\text{bottom}}} \quad (5)$$

The first of these terms depends on the fractional error in bottom type regression coefficient $\alpha(\lambda)_{\text{bottom}}$ when the wrong bottom type is selected in the processing chain of Figure 9. Using the regression coefficients for the muddy bottom and oyster shell bottom examples of Figures 5 and 6, we find that when a oyster shell bottom case pixel is mislabeled as the muddy bottom case, we would have $(\delta d)_{\alpha_{\text{oyster/mud}}} \approx 0.299d$, while for the case of a muddy bottom mislabeled as oyster shell bottom, we would have $(\delta d)_{\alpha_{\text{mud/oyster}}} \approx 0.427d$. Thus, at $d = 10$ cm, we find corresponding errors of 2.99 and 4.27, while at 100 cm, we obtain 29.9 and 42.7 cm. This is an extreme case, and a more likely kind of error would be confusion of the sand-silt bottom with the oyster shell/silt bottom. In this case, we would obtain an error of $(\delta d)_{\alpha(\lambda)_{\text{sand-silt/oyster-silt}}} \approx 0.1301d$, while for the reverse situation of oyster shell/silt bottom confused with sand-silt, we would have $(\delta d)_{\alpha(\lambda)_{\text{oyster-silt/sand-silt}}} \approx 0.1496d$. This more realistic error would yield an uncertainty of 1.30 and 1.50 cm, respectively, at $d = 10$ cm, while at $d = 100$ cm we would obtain 13.0 and 15.0 cm.

The second error term related to the bottom type, represented in Eq. (5), is independent of depth, depending only on the bottom type regression, in particular the difference in the regression offset term when an error in bottom type is made, scaled by the estimated slope of the regression of $\ln(R_{810})$ versus d . For an oyster shell bottom mislabeled as muddy bottom, we would have $(\delta d)_{\beta_{\text{oyster/mud}}} \approx 13.3$ cm while for muddy bottom mislabeled as oyster, we would have $(\delta d)_{\beta_{\text{oyster/mud}}} \approx 18.9$ cm. For the more realistic case of sand-silt bottom being confused with oyster shell-silt, we obtain $(\delta d)_{\beta(\lambda)_{\text{sand-silt/oyster-silt}}} \approx 0.055$ cm, and for oyster-silt mislabeled as sand-silt, we find $(\delta d)_{\beta(\lambda)_{\text{oyster-silt/sand-silt}}} \approx 0.064$ cm.

The confusion between muddy bottom and oyster shell bottom is not as likely in a scenario in which many different bottom types are present in the library, so these numbers obviously represent an upper bound since the oyster shell bottom is significantly brighter than the muddy bottom of the tidal creek bank. The second analysis above in which a sand-silt bottom and an oyster-silt bottom are confused is more likely. Nevertheless, the analysis of the extreme cases indicates the relative importance of selecting a good bottom type in this type of modeling. A more likely scenario is the situation in which the bottom type is more mixed, in which case the corresponding error estimates resulting from choosing one model at either extreme is somewhat reduced compared to the above analysis but still present. Therefore, a comprehensive set of representative bottom types becomes important so that the factor $\frac{\delta\alpha(\lambda)_{\text{bottom}}}{\alpha(\lambda)_{\text{bottom}}}$ which scales d in Eq. (4) will remain relatively small.

One final note concerning error analysis is that the total error in d , $(\delta d)_{tot}$, adds each of the error terms described above in quadrature:

$$(\delta d)_{tot} = \sqrt{(\delta d)_{R\lambda}^2 + (\delta d)_{\alpha_{bottom}}^2 + (\delta d)_{\beta_{bottom}}^2} \quad (6)$$

Thus, for the case of $d = 10$ cm with a 10% error in radiometric accuracy for an oyster shell bottom mistaken as a muddy bottom, the least likely bottom type error, we would derive an estimated total error of:

$$(\delta d)_{d=10\text{ cm}, \frac{(\delta R\lambda)}{R\lambda}=0.1, \text{oyster/mud}} = \sqrt{2.77^2 + 2.99^2 + 13.28^2} \approx 13.89 \text{ cm}, \quad (7)$$

while for the more realistic case of sand-silt bottom mistaken as oyster shell bottom we obtain:

$$(\delta d)_{d=10\text{ cm}, \frac{(\delta R\lambda)}{R\lambda}=0.1, \text{sand-silt/oyster}} = \sqrt{2.41^2 + 1.301^2 + 0.055^2} \approx 2.74 \text{ cm} \quad (8)$$

If the radiometric error increases to 20%, then the values in Eqs. (7) and (8) increase to 14.7 and 4.99 cm, respectively. At $d = 100$ cm, we find that:

$$(\delta d)_{d=100\text{ cm}, \frac{(\delta R\lambda)}{R\lambda}=0.1, \text{oyster/mud}} = \sqrt{2.77^2 + 29.92^2 + 13.28^2} \approx 32.85 \text{ cm} \quad (9)$$

while for the more realistic error of sand-silt mistaken as oyster shell bottom, we find:

$$(\delta d)_{d=100\text{ cm}, \frac{(\delta R\lambda)}{R\lambda}=0.1, \text{sand-silt/oyster}} = \sqrt{2.41^2 + 13.01^2 + 0.055^2} \approx 13.23 \text{ cm} \quad (10)$$

If the radiometric error increases to 20%, the uncertainty in Eq. (9) increases just slightly to 33.2 cm, while the uncertainty in Eq. (10) increases to just 13.87 cm.

To provide a comprehensive picture of the error budget, we generated a table of estimated errors as a function of depth for each of the possible types of error described above as a function of depth. Table 1 shows the total estimated error for a 1% radiometric uncertainty, while Table 2 shows the estimated error for a 10% radiometric uncertainty.

The results of Figure 12 suggest that even with the limited set of bottom types used in the retrieval presented here, we have obtained a reasonable level of accuracy, especially compared to the worst case scenario described earlier. In fact, the difference between the ideal retrieval and the mean retrieval mimics very closely the error rates that we described for the more benign error case of sand-silt being mistaken for oyster shell bottom. At $d = 10$ cm, for example, the mean bathymetric retrieval departs from the ideal case by just 1.4 cm and the standard deviation is 5.2 cm, while at $d = 98$ cm the mean bathymetric departs from the ideal case by just 8.3 cm, and the standard deviation is about 11.5 cm. For the region where our bathymetric retrieval works well, the 0–1 m depth range in Figure 12, we find a root mean square error (RMSE) of 13.7 cm over all depths in this range.

Known systematic sources of error include the fact that particular bottom types known to be in the imagery were not included in the model. The error budget, which establishes an upper bound for these errors, and the resulting errors depicted in Figure 12 indicate that we have achieved good results because we have measured bottom types that were both dark (muddy bottom) and reasonably bright (oyster shell bottom and sand-silt bottom). Thus, for example, even though *Ulva lactuca* was known to be in the region where validation was undertaken (Figures 6 and 11), its omission in the model still led to errors within our desired level of accuracy out to 1 m depth because the reflectance of this submerged aquatic vegetation (SAV) was likely somewhere within the range spanned by the three bottom types

Table 1
Estimated error in depth retrieval as a function of depth for a 1% radiometric uncertainty

depth (cm)	Total Error in Quadrature for a radiometric error of 0.01									
	10	20	30	40	50	60	70	80	90	100
oyster mislabelled mud	13.62	14.57	16.03	17.88	20.00	22.33	24.80	27.37	30.02	32.73
mud mislabelled oyster	19.43	20.79	22.87	25.51	28.54	31.86	35.39	39.06	42.84	46.71
sand-silt mislabelled oyster	1.32	2.61	3.91	5.21	6.51	7.81	9.11	10.41	11.71	13.01
oyster mislabelled sand-silt	1.52	3.01	4.50	5.99	7.48	8.98	10.47	11.97	13.47	14.96
sand-silt mislabelled mud	12.14	13.90	16.41	19.39	22.65	26.09	29.65	33.28	36.97	40.69
mud mislabelled sand-silt	19.92	22.80	26.92	31.81	37.16	42.80	48.63	54.59	60.64	66.75

Table 2
Estimated error in depth retrieval as a function of depth for a 10% radiometric uncertainty

depth (cm)	$\text{Total Error in Quadrature for a radiometric error of 0.1 } (\delta d)_{tot} = \sqrt{(\delta d)_{R_x}^2 + (\delta d)_{\rho_{bottom}}^2 + (\delta d)_{\rho_{bottom}}^2}$									
	10	20	30	40	50	60	70	80	90	100
oyster mislabeled mud	13.89	14.83	16.27	18.09	20.19	22.50	24.95	27.51	30.15	32.85
mud mislabeled oyster	19.82	21.16	23.21	25.81	28.81	32.10	35.60	39.25	43.02	46.87
sand-silt mislabeled oyster	2.74	3.55	4.59	5.74	6.94	8.17	9.42	10.69	11.96	13.23
oyster mislabeled sand-silt	3.15	4.08	5.27	6.59	7.98	9.39	10.83	12.28	13.74	15.21
sand-silt mislabeled mud	12.38	14.10	16.59	19.54	22.78	26.20	29.74	33.36	37.04	40.77
mud mislabeled sand-silt	20.30	23.14	27.21	23.05	37.37	42.98	48.79	54.73	60.76	66.87

used in the retrieval. However, the depth dependence predicted by the error budget (Eq. (4)) is observed in our results where the error bars are seen to increase with increasing depth. This latter fact was attributable in the error budget to mistakes in bottom type delineation which form the early stages of the processing chain defined in Figure 9. This is consistent with the fact that we did not use a comprehensive set of bottoms. Furthermore, mixed bottom types also fall into this category of potential error, which would have the same depth dependence given in Eq. (4). Even with these limitations, we still achieved an RMSE depth of error of 13.7 cm in the 0–1 m depth range, which was within our established goal.

Conclusions

We have shown the potential of near infra-red features centered near 810 nm and 720 nm for retrieving very shallow water bathymetry (< 1–2 m depth). Because this portion of the spectrum is predominantly influenced by water absorption (depth) and the reflectance of the bottom, effects of suspended constituents have only a secondary contribution, allowing us to use a set of simple regressions based on bottom type rather than a full radiative transfer model in the very shallow water limit. Hydrolight simulations confirmed the validity of this assumption, and tests of this model, using a limited set of *in situ* spectral reflectance samples versus depth to establish appropriate regressions, produced a result with reasonable error bounds, an RMSE error of 13.7 cm in the 0–1m depth range. An error budget was derived and upper bounds on potential error were derived. These results emphasize the importance of a well-represented set of bottom types, which is one of the most important potential sources of error for our simplified approach depicted in Figure 9. The importance of good sensor calibration and atmospheric correction was also apparent in the error budget, although the total error is more sensitive to mistakes in estimated bottom type.

Operational LIDAR systems such as SHOALS do not produce reliable retrievals in the very shallow waters; therefore, in joint HSI/LIDAR platforms, such as CHARTS, the new approach could fill a gap in bathymetric retrieval in the very shallow water limit.

Acknowledgement

The NRL authors gratefully acknowledge platform support from the Office of Naval Research. This article was also funded by the National Geospatial-Intelligence Agency (NGA). The opinions, views, and conclusions found within the article do not necessarily reflect those of the U.S. Department of Defense or the NGA.

References

- Bachmann, C. M., M. H. Bettenhausen, R. A. Fusina, T. F. Donato, A. L. Russ, J. W. Burke, G. M. Lamela, W. Joseph Rhea, B. R. Truitt, and J. H. Porter. 2003. A credit assignment approach to fusing classifiers of multiseason hyperspectral imagery. *IEEE Transactions on Geoscience and Remote Sensing* 41:2488–2499.
- Bachmann, C. M., C. R. Nichols, M. J. Montes, R.-R. Li, P. Woodward, R. A. Fusina, W. Chen, M. Crawford, W. Kim, V. Mishra, J. Monty, K. McIlhany, D. Korwan, D. Miller, E. Bennert, G. Smith, D. Gillis, G. Marmorino, J. Sellars, C. Parrish, A. Schwarzschild, and B. Truitt. 2008. Remote sensing retrieval of substrate bearing strength from hyperspectral imagery at the Virginia Coast Reserve (VCR'07). Multi-Sensor Campaign, Proc. IGARSS'08.
- Curcio, J. A., and C. C. Petty. 1951. The near infrared absorption spectrum of liquid water. *Journal of Optical Society of America* 41:302–304.

- Ebrite, S., B. Pope, and W. J. Lillycrop. 2001. A multi-agency solution for coastal surveys—SHOALS in the Pacific. *Oceans 2001 Proceedings*, 2:1204–1211.
- Guenther, G. C., M. W. Brooks, and P. E. LaRocque. 2000. New capabilities of the SHOALS airborne lidar bathymeter. *Remote Sensing of Environment* 73:247–255.
- Kruse, F. A., A. B. Lefkoff, J. W. Boardman, K. B. Heidebrecht, A. T. Shapiro, P. J. Barloon, and A. F. H. Goetz. 1993. The spectral image processing system (SIPS)—interactive visualization and analysis of imaging spectrometer data. *Remote Sensing of Environment* 44:145–163.
- Lee, Z., K. L. Carder, S. K. Hawes, R. G. Steward, T. G. Peacock, and C. O. Davis. 1994. Model for the interpretation of hyperspectral remote-sensing reflectance. *Applied Optics* 33:5721–5732.
- Lee, Z., K. L. Carder, C. D. Mobley, R. G. Steward, and J. S. Patch. 1999. Hyperspectral remote sensing for shallow waters: 2. Deriving bottom depths and water properties by optimization. *Applied Optics* 38:3831–3843.
- Lee, Z., K. L. Carder, R. F. Chen, and T. G. Peacock. 2001. Properties of the water column and bottom derived from airborne visible infrared imaging spectrometer (AVIRIS) data. *Journal of Geophysical Research* 106:11639–11651.
- Mobley, C. D. 1994. *Light and water: Radiative transfer in natural waters*. San Diego, CA: Academic Press.
- Mobley, C. D., W. P. Bissett, J. H. Bowles, C. O. Davis, T. V. Downes, A. Gleason, D. D. R. Kohler, R. A. Leathers, E. M. Lochard, M. J. Montes, R. P. Reid, and L. K. Sundman. 2005. Interpretation of hyperspectral remote-sensing imagery via spectrum matching and look-up tables. *Applied Optics* 44:3576–3592.
- Mobley, C. D., and L. K. Sundman. 2000. *Hydrolight 4.1 technical documentation*. Seattle: Sequoia Scientific, Inc.
- Montes, M. J., B.-C. Gao, and C. O. Davis. 2004. NRL atmospheric correction algorithms for oceans: Tafkaa user's guide. Naval Research Laboratory memorandum report 7230-04-8760.
- Smith, R. A., J. L. Irish, and M. Q. Smith. 2000. *Airborne LIDAR and airborne hyperspectral imagery: A fusion of two proven sensors for improved hydrographic surveying*. Proceedings of the Canadian Hydrographics Conference 2000.
- White, S. 2007. *Utilization of LIDAR and NOAA's vertical datum transformation tool (VDatum) for shoreline delineation*. Proceedings of the MTS/IEEE Oceans 2007 Conference.
- Yang, E., P. LaRocque, G. Guenther, D. Reid, W. Pan, and K. Francis. 2007. *Shallow water depth extraction—progress and challenges*. Proceedings of the 2007 U.S. Hydrographic Conference, May 14–18, in Norfolk, Virginia.